Available online at www.sciencedirect.com
SCIENCE DIRECT
C. R. Physique 6 (2005) 105–116
COMPTES RENDUS PHYSIQUE
http://france.elsevier.com/direct/COMREN/

Self-organization on surfaces/Auto-organisation sur les surfaces

Nanometric artificial structuring of semiconductor surfaces for crystalline growth

J. Eymery [a,*], G. Biasiol [b,1], E. Kapon [b], T. Ogino [c]

[a] *Équipe mixte CEA-CNRS-UJF « Nanophysique et Semiconducteurs », CEA/DRFMC/SP2M, 17, rue des Martyrs, 38054 Grenoble cedex 9, France*
[b] *Laboratory of Physics of Nanostructures, Institute of Quantum Electronics and Photonics, Swiss Federal Institute of Technology, Lausanne, CH-1015 Lausanne, Switzerland*
[c] *Department of Electrical and Computer Engineering, Yokohama National University, Tokiwadai 79-5, Hodogayaku, 240-8601 Yokohama, Japan*

Available online 12 January 2005

Presented by Guy Laval

Abstract

The coupling of standard self-organization methods with surface artificial nanostructuring has recently emerged as a promising technique in semiconductor materials to control simultaneously the size distribution, the density and the position of epitaxial nanostructures. Some physical aspects of the morphology and elastic strain engineering are reviewed in this article. The emphasis is on the effects of capillarity, growth rate anisotropy, strain relaxation and entropy of mixing for alloys. The interplay among these driving forces is first illustrated by III–V compound semiconductor growth on lithographically patterned surfaces, then by germanium growth on implanted substrates and nanopatterned templates obtained by chemical etching of buried strain dislocation networks. ***To cite this article: J. Eymery et al., C. R. Physique 6 (2005).***

Résumé

Structuration artificielle de surfaces de semi-conducteurs pour la croissance cristalline. Le couplage de méthodes classiques d'auto-organisation avec des nanostructurations artificielles de surfaces s'est récemment avéré être une excellente technique dans les matériaux semi-conducteurs pour contrôler simultanément la taille, la densité et la position de nanostructures épitaxiées. Certains aspects physiques concernant l'ingénierie de la morphologie et de la contrainte élastique sont passés en revue dans cet article. L'accent est mis sur les effets de capillarité, d'anisotropie de la vitesse de croissance, de relaxation de contrainte et d'entropie de mélange pour les alliages. L'interaction entre ces différentes forces motrices est illustrée en premier par la croissance de composés de semi-conducteurs III–V sur des surfaces obtenues par lithographie, puis par la croissance de germanium sur des substrats implantés et sur des surfaces nanostructurées obtenues par attaque chimique de réseaux de dislocations enterrées. ***Pour citer cet article : J. Eymery et al., C. R. Physique 6 (2005).***

Keywords: Surface nanopatterning; Self-assembling; Epitaxial growth; Strain and curvature engineering

* Corresponding author.
E-mail address: jeymery@cea.fr (J. Eymery).
[1] Present address: Laboratorio TASC-INFM, SS14, Km 163.5, Basovizza, 34012 Trieste, Italy.

1631-0705/$ – see front matter
doi:10.1016/j.crhy.2004.11.006

Mots-clés : Nanostructuration de surface ; Auto-organisation ; Croissance épitaxiale ; Ingénierie de contrainte et de courbure

1. Introduction

The development of industrial processes for patterning semiconductors on the nanometric scale is one of the main nanotechnology challenges to obtain templates for producing low-dimensional quantum nanostructures (quantum wells, wires and dots) by direct epitaxial growth. The standard *top-down approach* of the integrated circuit manufacturing industry uses optical lithographic techniques giving already access to feature sizes as small as one hundred of nanometers. Smaller features sizes of about tens of nanometers are produced using electron beam lithography or scanned ion beams, at the expense of processing time. The nano-imprint technique [1] enables a parallel nanoscale processing capability by using well-resolved techniques, such as electron beam lithography to create the master stamp that is embossed on polymer substrates before hardening and etching processes. One can also produce an assembly of self-organized nanostructures with a predefined nanometric size, and then addressing these objects by methods that are more conventional. A famous example in the field of semiconductors consists of the hetero-epitaxial growth of self-organizing three-dimensional islands used in memories and laser applications. This method suffers generally from poor size homogeneity and density control. The *bottom-up approach* has proposed to steer the nanostructures nucleation by using spontaneous surface patterns such as specific reconstructions [2], steps at vicinal surfaces [3] or relaxed templates with dislocations [4]. Unfortunately, simultaneous control of the size distribution, density and position of the structures in the nanometer range has not yet been achieved, in general. Indeed, it is very difficult to find versatile methods that can be applied to a large range of feature sizes over large areas. Several examples shown in this article will demonstrate that the coupling of artificial surface nanoprepatterning with self-organization process is a promising technique that solves the spatial control of nanostructure positioning. This approach, at the junction of top-down and bottom-up methods, will be probably strongly developed in future semiconductor nanotechnology.

The first part of this article will report on the physical ingredients driving 'seeded' self-organization in nanopatterned surfaces. These effects will be illustrated with III–V compound semiconductor growth on lithographically patterned surfaces, leading to the formation of self-organized quantum wires and dots. The second part of the article will be focused on emerging nanopatterning methods compatible with the microelectronics technology for obtaining surface artificial nanostructuration. Two ways based on the use of implantation and ion engineering and chemical etching of buried strain networks will be especially discussed. The last part will conclude on the interest of the nanometric artificial structuration of semi-conductor surfaces.

2. Physical ingredients to steer semiconductor self-organization and growth on nanopatterned surface: nonplanar epitaxy

2.1. Generalities

According to the Nernst–Einstein relation, the driving force for surface homoepitaxial growth depends on the local gradient of the chemical potential μ (see [5], and the contribution of O. Pierre-Louis in this issue). The surface atomic flux j is given by

$$j = -\frac{nD}{k_{\mathrm{B}}T}\frac{\partial \mu}{\partial s} \tag{1}$$

where n is the adatom density, D the diffusion coefficient and ∂s an infinitesimal segment of the surface profile. The local growth rate can then be expressed by means of the continuity equation as:

$$R = \Omega_0\left(J_0 - \frac{\partial j}{\partial s}\right) = \Omega_0\left(J_0 + \frac{nD}{k_{\mathrm{B}}T}\frac{\partial^2 \mu}{\partial s^2}\right), \tag{2}$$

where Ω_0 is the volume of the unit cell and J_0 is the (local) deposition flux, which includes arrival, decomposition and chemisorption of the growth species arriving from the material sources.

Following the pioneering works of Herring and Mullins [6,7], μ is written for a one-dimensional patterned surface as $\mu(x) = \mu_0 + \Omega_0[\gamma(\theta) + \gamma''(\theta)]\kappa(x) + \Omega_0 E_{\mathrm{s}}(x)$. μ_0 is the chemical potential of the flat and unstressed surface, $\gamma(\theta)$ is the surface free energy that depends on orientation θ, $\kappa(x)$ is the surface curvature (negative for concave morphology), and $E_{\mathrm{s}}(x)$ is a local strain energy that can take into account relaxation effects. This chemical potential formulation clearly shows that surface curvature and strain energy are playing important roles in quantum wire and dot location [8–10]. In the case of a multicomponent system, treated as an ideal solution, the chemical potential must also take into account the entropy of mixing of the system and, for each component i of the alloy of composition x_i, it assumes the form [11]

$$\mu_i(x) = \mu_{i,0} + \Omega_{i,0}\big[\gamma(\theta) + \gamma''(\theta)\big]\kappa(x) + \Omega_{i,0}E_{\mathrm{s}}(x) + \Omega_{i,0}k_{\mathrm{B}}T\ln x_i(x), \tag{3}$$

where x_i is the mole fraction of the component. The last term reflects the tendency of the system to maximize the compositional disorder on the surface.

In homoepitaxial growth, the curvature term will force adatoms to diffuse towards concave morphologies (*capillarity* fluxes, in analogy with the similar phenomenology for fluids) whereas the elasticity term favors a strong relaxation close to convex morphologies (edge, apex); the entropy term drives adatoms to diffuse towards areas where their concentration in the alloy is lower. The heteroepitaxial growth will also depend on these three ingredients, the elastic energy term taking also into account the lattice mismatch between the elements. An interesting example of strain engineering is given by the InAs/GaAs system [12,13] where two distinct growth regimes can be observed from InAs islands grown on patterned GaAs substrates. In the case of direct growth, all the islands form between mesas, whereas the incorporation of an $In_{0.2}Ga_{0.8}As$ stressor layer before the overgrowth of the GaAs patterned substrate leads to well-controlled nucleation of the dots at the top of the mesas.

Self-limiting growth can be realized locally or globally, if conditions exist that lead to a steady state and uniform growth rate distribution in adjacent areas on the growing surface. Moreover, any perturbation to epitaxial growth (e.g., material composition or growth conditions) should cause growth transients leading to a new self-limiting state. This is formalized analytically in the continuity equation (2): surface fluxes driven by chemical potential gradients must coexist with a deposition-rate distribution $\Omega_0 J_0(x)$ (given, e.g., by the presence of various surface orientations with different reaction rates for the adsorbed species), and should be directed towards areas with lower growth rates. In this way, surface fluxes can compensate for deposition rates differences, and yield a uniform distribution of the overall growth rate.

2.2. Application example: self-ordered semiconductor nanostructured by nonplanar epitaxy

Seeded self-organization of semiconductor quantum wires (QWRs) has been achieved by epitaxial growth of (In)GaAs/AlGaAs quantum wells (QWs) on a sawtooth-shaped GaAs surface [14–18]. More recently, the technique has been extended to realize self-organized quantum dots (QDs), by growth on a matrix of pyramidal recesses [19].

The fabrication method for QWRs is outlined in the cross-sectional schematics of Fig. 1. A GaAs (100) substrate is covered with a periodic array of photoresist or poly (methyl methacrylate) (PMMA) stripes defined by optical, holographic or e-beam lithography, with a period from a few 100 nm to a few μm (a), and then wet-etched into an array of V-shaped grooves (b). Epitaxial growth by Metalorganic Chemical Vapor Deposition (MOCVD) of a GaAs/AlGaAs QW results in the formation of an array of parallel QWRs at the bottom of the grooves, due to a local thickening of the QW (c).

Fig. 2(a) shows a transmission electron microscopy (TEM) cross-section of an AlGaAs/GaAs multiple QW structure, grown by low pressure MOCVD on a GaAs substrate, pre-patterned with an array of V grooves oriented along the $[0\,1\,-1]$ direction with a period of 0.5 μm along $[0\,1\,1]$. The GaAs QWs allow one to follow the evolution of the nonplanar profile as growth proceeds [16]. The $\{1\,1\,1\}$ A-oriented sidewalls of the groove evolve into high-index planes, while at the top of the mesas a faceted structure emerges, constituted of a central (100) facet surrounded by two $\{3\,1\,1\}$A ones. The bottom of the grooves can be better seen in the details of Fig. 2(b): when the GaAs QW is deposited on the AlGaAs barrier, the profile becomes wider and a faceted structure with the same orientations as on the top emerges. In the same zone, some tens of nm wide, the QW thickens with respect to the sidewalls; this thickening causes a lateral quantum confinement for charge carriers, and thus the formation

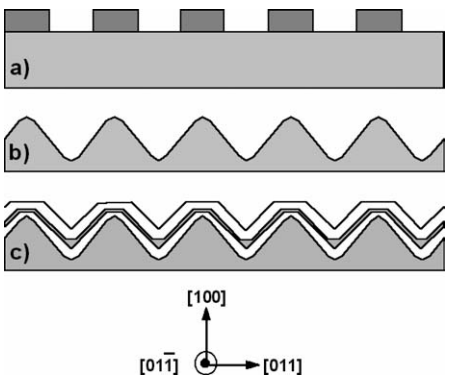

Fig. 1. Cross-sectional schematics of the fabrication phases of QWRs grown on nonplanar substrates: (a) Deposition of patterned photoresist or PMMA stripes on a GaAs (100) substrate; (b) Definition of an array of V grooves by wet chemical etching; (c) Growth of a GaAs/AlGaAs QW structure with the formation of QWRs at the bottom of the grooves.

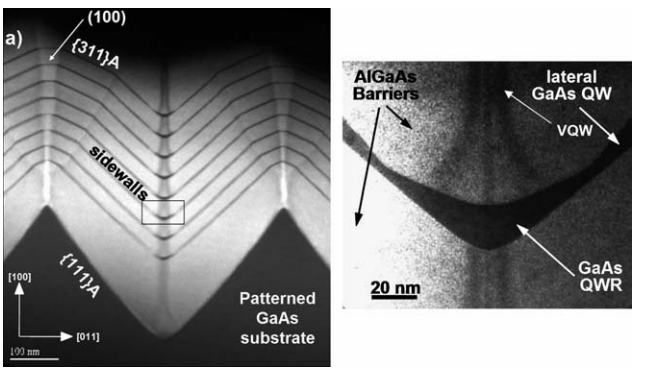

Fig. 2. (a) Cross sectional TEM image of a V-groove where a GaAs/AlGaAs multiple QW structure was grown by low pressure MOCVD. Darker contrast corresponds to GaAs layers, while lighter ones correspond to AlGaAs. Nanofacets forming in different areas of the groove are indicated. (b) Detail of the bottom region, showing the formation of a crescent-shaped QWR and of a VQW in the AlGaAs barrier.

of a QWR [16]. During AlGaAs deposition, the TEM contrast at the bottom reveals the formation of a Ga-rich phase in the QWR area propagating vertically, and clearly composed of three branches corresponding to the (1 0 0) and {3 1 1}A facets [20]. Quantum confinement has been observed also in this structure, thus termed Vertical Quantum Well (VQW) [21]. The width of the VQW allows following the evolution of the bottom profile after QWR growth: the widened profile narrows again and recovers the initial width before deposition of GaAs. This *self*-limiting behavior makes possible the formation of a multiple array of stacked, identical QWRs to themselves, as seen in Fig. 2(a). Note that, contrary to the bottom, the top profile does not evolve in a self-limiting fashion, since it expands continuously, until complete planarization of the grooves, thus limiting the number of QWRs that can be fit in the structure.

This self-limiting growth behavior can be interpreted in terms of the model outlined above, thanks to a profile-stabilizing interplay of curvature-related capillarity fluxes and deposition rate distribution in the bottom region [22,23]. Note that, since the AlGaAs/GaAs system is lattice-matched, the strain-related term in the surface chemical potential (see Eq. (3)) can be neglected, while the entropy of mixing term is relevant only to AlGaAs alloys, and not to the GaAs binary compound. We will start the discussion taking into account the capillarity term alone (that can account qualitatively for AlGaAs growth as well), and consider later the correction due to the entropy of mixing effects. For a fully faceted profile, such as that forming here, the capillary term must be modified in a suitable way, to avoid divergences of the second derivative of the surface free energy. According to the formulation of Herring [24], the chemical potential for a facet with surface area A can be written as

$$\mu = \mu_0 + \frac{\Omega_0}{A}\sum_{i=1}^{N}(\gamma_i \csc\theta_i - \gamma_0 \cot\theta_i)a_i,$$

where the sum runs over all the neighboring facets, each forming with A an edge of length a_i and an angle θ_i.

For simplicity of formulation, we will suppose that both the bottom and top regions are single, (1 0 0)-oriented facets, separated by a sidewall plane (taking into account the full fine structure of the profile adds only mathematical complications, without providing physical information). For such a faceted surface profile shown in Fig. 3, the chemical potential defined above becomes for the top (t), bottom (b) and sidewall (s) planes [25]:

$$\mu_{t,b} = \mu_0 \pm \gamma\Omega_0/l_{t,b}; \qquad \mu_s = \mu_0, \tag{4}$$

where θ is the sidewall orientation, $\gamma = 2(\gamma_s/\sin\theta - \gamma_b/\tan\theta)$, $+(-)$ refers to the top (bottom) (100)-oriented facet, $l_t(l_b)$ is the width of the top (bottom) facet, and $\gamma_t = \gamma_b$. Note that $\mu_t > \mu_0$, and $\mu_b < \mu_0$, (see Fig. 3(c)). This chemical potential profile determines adatom capillarity fluxes j towards the bottom of the groove, which increase as the profile becomes sharper. The growth rates R_i $(i = t, b, s)$ at the different facets (along the growth direction) are derived from equation (4) using the Nernst–Einstein relation (1) and the diffusion Eq. (2). Here the gradients are approximated by differences between the values of the relevant quantities on the two boundaries of each facet. Using in Eq. (2) the deposition rates $\Omega_0 J_i = \Omega_0 J_0 \cdot r_i$ on each facet in the absence of capillarity fluxes, with $\Omega_0 J_0$ being the 'nominal' deposition rate on a planar (100) reference sample, we obtain [22]:

$$R_{t,b} = \Omega_0 J_0\left(r_b \pm r_s \frac{C}{l_{t,b}^3}\right); \qquad R_s = \Omega_0 J_0 r_s, \tag{5}$$

where $C = 2\Omega_0 D_s \tau\gamma/k_B T$, D_s is the diffusion coefficient on the sidewalls, τ is the lifetime for adatom incorporation (adatom desorption is neglected), and $r_t = r_b$, since these facets have the same crystallographic orientation.

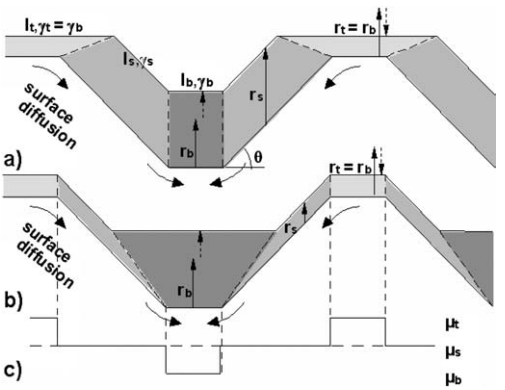

Fig. 3. Schematic groove profiles composed of three facets (not to scale). (a) Evolution of the growth front as commonly observed in MOCVD. (b) The same for MBE. (c) Chemical potential at each facet [22].

Self-limiting evolution is achieved at the top or at the bottom if the corners between the sidewalls and the top (bottom) facets propagate in the growth direction, i.e., when $R_t = R_s$ ($R_b = R_s$). Using Eq. (5), this defines the self-limiting widths of the top and bottom facets $l^{sl}_{t,b}$ as:

$$l^{sl}_t = \left(Cr_s/(-\Delta r)\right)^{1/3}; \qquad l^{sl}_b = (Cr_s/\Delta r)^{1/3}, \tag{6}$$

with $\Delta r = r_s - r_{t,b}$ representing the growth rate anisotropy. Thus, to obtain self-limiting growth at the top (bottom) of the groove, Δr must be negative (positive). For $\Delta r > 0$ the additional, capillarity-induced growth rate (dashed arrow in Fig. 3(a)) adds to the intrinsic one r_b to exactly balance r_s, since $r_s > r_b$. On the other hand, capillarity leads to a decrease of the top growth rate and therefore to an expansion of the top facet. This is the behavior observed in the MOCVD growth on patterned profiles shown in Fig. 2. Note that, for $\Delta r < 0$, exactly the opposite behavior is expected (see Fig. 3(b)). This has been observed in Molecular Beam Epitaxy (MBE) growth of GaAs/AlGaAs on corrugated (1 0 0) substrates, where self-limiting formation of QWRs at the top of the mesas has been obtained [18]. This different behavior for MOCVD and MBE, which is explained in the present model as due to the opposite sign of Δr, is a result of the higher dissociation rate of the precursors during MOCVD on the densely stepped groove sidewalls. MBE growth, on the other hand, leads to slowly growing {1 1 1}A or B sidewalls. Finally, the possibility of a *global* self-limiting behavior throughout the whole of the grooved profile is excluded by the model (nor has ever been experimentally observed), since either the case $\Delta r > 0$ or $\Delta r < 0$ can be realized during growth.

In an alloy, for a given profile (i.e. for a given chemical potential gradient), Eq. (1) predicts that capillarity fluxes towards concave regions, being proportional to the diffusion coefficient D, are larger for species with larger surface diffusion. This explains qualitatively the formation of the Ga-rich VQW at the bottom of the grooves (and as well of the Al-rich region that can be seen as a lighter grayscale at the top of the mesas in Fig. 2(a), forming in particular cases a 'vertical quantum barrier' [26]). This compositional non-uniformity increases the entropy of mixing of the surface. We will now examine the effects of the related term in Eq. (3) on the self-limiting profile, limiting the discussion to the bottom VQW. The (lower) Al mole fraction at the bottom facet can be expressed empirically as $x_b = x/[x(1-k)+k)]$, where x is the mole fraction at the nearby sidewalls, and k is a parameter larger than one, measured to be 1.81 ± 0.05 for MOCVD growth at 700 °C. Using this variation, the growth rates at the bottom facet assume the form

$$\begin{aligned} R^A_b &= x\Omega_0 J_0\left[r^A_b + \Delta r^A\left(\frac{l^{sl}_{b,A}}{l_b}\right)^3 + 2\left(\frac{L^A_s}{l_b}\right)^2 \ln\big(x(1-k)+k\big)\right], \\ R^G_b &= (1-x)\Omega_0 J_0\left[r^G_b + \Delta r^G\left(\frac{l^{sl}_{b,G}}{l_b}\right)^3 + 2\left(\frac{L^G_s}{l_b}\right)^2 \ln\frac{x(1-k)+k}{k}\right], \end{aligned} \tag{7}$$

with the indexes A and G referring to AlAs and GaAs growth, respectively. By assuming that the composition on the sidewalls is equal to the nominal one, the equalization of the growth rates on the different facets, leading to a self-limiting bottom profile l^{sl}_b yields, for an alloy:

$$\begin{aligned} &\frac{a}{(l^{sl}_b)^3} + \frac{b}{(l^{sl}_b)^2} = \Delta r(x), \quad \text{with} \\ &\begin{cases} a = x\Delta r^A (l^{sl}_{b,A})^3 + (1-x)\Delta r^G (l^{sl}_{b,G})^3, \\ b = 2\left(x(L^A_s)^2 \ln\big(x(1-k)+k\big) + (1-x)(L^G_s)^2 \ln\dfrac{x(1-k)+k}{k}\right), \\ \Delta r(x) = x\Delta r^A + (1-x)\Delta r^G, \end{cases} \end{aligned} \tag{8}$$

where $l^{sl}_{b,A}$ and $l^{sl}_{b,G}$ denote the self-limiting facet widths for the binary AlAs and GaAs compounds, respectively. The self-limiting profile of an alloy is therefore determined by the interplay among the effects of capillarity (a), entropy of mixing (b) and growth rate anisotropy ($\Delta r(x)$).

The approach outlined above can account for the phenomenology of self-ordering in nonplanar epitaxy; furthermore, it can as well be compared *quantitatively* to the observed growth profiles, and used to gain knowledge on some kinetic parameters. Assuming an Arrhenius temperature dependence of $D_s = D_0 \exp(-E_B/k_B T)$, with E_B the diffusion barrier on the sidewalls in the direction perpendicular to the groove axis, Eq. (6) predicts a temperature dependence essentially of the form $\exp(-E_B/3k_B T)$ for l^{sl}_b in a single binary compound. For alloys, the T dependence of l^{sl}_b, given by Eq. (8), is more complicated, but shows qualitatively a similar behavior deriving from the Arrhenius form of $l^{sl}_{b,A}$, $l^{sl}_{b,G}$, L^A_s and L^G_s. The measured variation of the bottom self-limiting profile with T is shown in Fig. 4(a) for GaAs and $Al_xGa_{1-x}As$ with $x = 0.19$, 0.29 and 0.47 and for 600 °C $< T <$ 750 °C. The Arrhenius fit for GaAs gives $E^G_B = 1.9 \pm 0.3$ eV, while least squares fits of the $Al_xGa_{1-x}As$ profiles yield, consistently for the three compositions, $E^A_B = 2.3 \pm 0.2$ eV. This difference between the GaAs and AlAs diffusion barriers is consistent with stronger Al–As bonds, as compared with Ga–As ones, giving a much larger diffusion length for Ga,

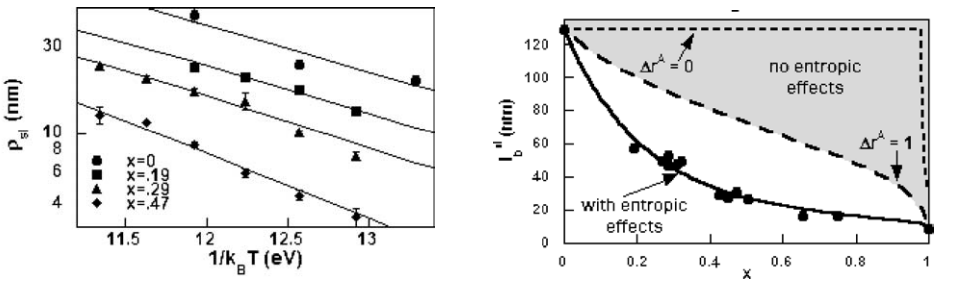

Fig. 4. (a) Arrhenius plot of the bottom self-limiting width for $Al_xGa_{1-x}As$ alloys with composition ranging from $x = 0$ to $x = 0.47$. As the bottom facets could not be readily resolved for very narrow (< 10 nm) profiles, we have characterized the groove width in that case by the radius of curvature ρ_{sl} for a hyperbola tangent to the surface; ρ_{sl} is related to l_b^{sl} via a simple geometrical factor. Solid lines are fits of the experimental data with Eq. (7) (GaAs) and Eq. (8) ($Al_xGa_{1-x}As$). (b) Measured as a function of x for $T = 700\,^{\circ}C$. The solid line is a fit of the data with the function defined in Eq. (8). Long-dashed and short-dashed lines, delimiting the shaded region, represent the hypothetical dependence of l_b^{sh} on x by neglecting the entropy of mixing effects, and setting $\Delta r^G = 0.22$ and $\Delta r^A = 1$ or $\Delta r^A \to 0$, respectively (see text for details) [22].

with respect to Al. This is in qualitative agreement with findings on planar (100) surfaces both for MBE and MOCVD; however more quantitative comparisons would not be reliable, due to the wide range of experimental results reported in the literature.

The importance of entropy of mixing effects can be appreciated by modeling the dependence of the alloy self-limiting profile as a function of the Al composition. The circles in Fig. 4(b) show the measured profiles for $Al_xGa_{1-x}As$ alloys (circles) at $T = 700\,^{\circ}C$. These values can be fitted with the solution of Eq. (8), where the GaAs and AlAs self-limiting widths and Δr can be fixed to their measured values. At 700 °C it was found that $l_{b,G}^{sl} = 129 \pm 3$ nm and $l_{b,A}^{sl} = 9.1 \pm 0.1$ nm. Regarding the growth rate anisotropies, only Δr^G was measured and found to be largely independent of T ($\Delta r^G = 0.22 \pm 0.05$); however, the fit is almost insensitive to Δr^A in the whole interval $0 \leqslant \Delta r^A \leqslant 1$. Since $(L_s^G)^2 \gg (L_s^A)^2$, the AlAs term appearing in the term b in Eq. (8) can be neglected, thus any entropy-related compositional variations in the VQW are ascribed to *Ga diffusion* away from the bottom. This leaves L_s^G as the only fit parameter, found to be $L_s^G = 175 \pm 20$ nm. This value is lower than that estimated on (1 0 0) surfaces, [27], as expected for a densely stepped, high-index facet. To estimate the importance of the entropy effects, we also represent by the shaded area in Fig. 4(b) the best fits for l_b^{sl} neglecting the term b in Eq. (8) and setting $\Delta r^G = 0.22$, with the boundaries corresponding to the extreme cases $\Delta r^A = 1$ (long-dashed line) or $\Delta r^A = 0$ (short-dashed line). The measured alloy self-limiting widths are systematically smaller than the ones predicted neglecting the entropy term.

Finally, by combining the relations that describe bottom growth rates and self-limiting profiles, it is possible to model quantitatively the evolution from an AlGaAs self-limiting profile to the GaAs one, and back to the AlGaAs one [22,23]. The model developed above can be employed to elucidate the self-ordering of quantum nanostructures relying on self-limiting surface evolution. The fact that the self-limiting width increases with the group-III diffusion length explains directly the self-ordering of crescent-shaped QWRs grown on V-grooves. Thus, growing a low bandgap semiconductor layer characterized by longer L_s on a self-limiting higher bandgap surface (e.g., GaAs on AlGaAs, InGaAs on GaAs) leads to the expansion of the bottom facets and the experimentally observed formation of a QWR. The same model could be extended to a two-dimensional profile to explain the self-formation of QD structures obtained by MOCVD in inverted tetrahedral pyramids [19].

3. Artificial surface structuration at the nanometer scale

3.1. New lithographic methods to shrink dimensions

At the nanometer scale, the use of curvature to steer the self-organization motivates the development of new high-resolution nanopatterning processes based on the *bottom-up* approach and compatible with very large scale integration (VLSI).

Quite recent methods transfer the order obtained by spontaneous organization of polymer phases. As an example, the self-assembled phase separation under annealing of diblock copolymers – a mixture of polystyrene and PMMA molecules – onto a thermal oxide on a silicon substrate leads to nanoscale PMMA cylinders in a polystyrene matrix. Removing the PMMA with an organic solvent leaves a porous polystyrene film acting as a sacrificial layer to define nanocrystals or to develop a template for growth [28]. More generally, surface relief patterns on polymers are also successfully employed as a substrate for a template–directed crystal assembly with the control of spacing and depth of the grooves [29]. Capillary force, depending on the surface morphology, works, for example, as a driving force for making dense colloidal arrays obtained by chemical synthesis. These colloids can then be used directly for their individual physical properties, for example ultimate magnetic recording [30], but

also as a mask for reactive ion etching to obtain nanopillars [31] or for selective deposition of metals or semiconductors, as it has been demonstrated for latex nanospheres [32,33].

More recently, biomimetic nanofabrication has been developed to obtain versatile substrates for templated assembly of organized arrays of molecules as well as metal and semiconductor nanoparticles. Some examples use bacterial surface protein layers (S-layers) to form crystalline two-dimensional (2D) structures composed of a single (glycol-) protein species [34]. These arrays have a well-defined symmetry and the unit cell dimensions can be controlled in the range 3–30 nm with the protein strain.

Another nanopatterning method that can be applied on large areas uses the instability resulting from the dependence of the erosion rate of an ion beam on the surface curvature: a protusion erodes more slowly than a depression [35]. A convenient choice of the angle of incidence can create regular surface morphologies ranging from ripples to pyramids. Under normal incidence, isotropic patterns of nanometer-scale mounds form on Si [36] and GaSb or InSb [37]. These structures should be used in the near future for overgrowth positioning after removing structural surface defects.

Nanoscale strain patterning is also developed to overcome the size limitation of optical lithography. In the case of coherently grown nanostructures, the elastic coupling between the deposited nanostructure and the surface strain field strongly modifies the local strain energy $E_s(x)$ involved in the chemical potential. It may play a more important role than atomic steps or other surface defects.

3.2. Implantation and ion engineering

In this section, we describe strain engineering on Si substrates as a way to control self-assembled Ge nanostructures. Nucleation sites of the Ge dots on Si(0 0 1) are sensitive to the strain field of the substrate. This was shown in multilayers consisting of Ge-island layers and Si-spacer layers [see Ref. [38] and the contribution of G. Springholz in this issue]. In this case, Ge island nucleation takes place preferentially just above the embedded Ge islands. A method based on this mechanism has been developed to artificially control the strain distribution on Si surfaces using oxygen ion implantation [39]. The process is illustrated in Fig. 5. Oxygen ions were implanted through an oxide mask formed by the standard Si process, and then the substrates were annealed at 1325 °C to form buried oxide inclusions. Since the volume of a given inclusion is approximately double its Si content prior to implantation, a strain field is generated by the oxide inclusions. In these experiments, oxygen ions were implanted at energy of 180 keV. Under this condition, the implanted oxygen atoms were distributed at depths of 200–500 nm, and SiO_2 inclusions were produced at a depth of about 300 nm after a high-temperature annealing. The dose was 5×10^{16} cm^{-2}. The inclusions are too small to be observed in standard transmission electron microscopy cross-section, but atomic force microscopy shows that the surface rose about 1–2 nm in the implanted regions. Therefore, point stressors can model such inclusions in the calculations of the total strain function. The SiO_2 inclusions are thermally stable and therefore any subsequent processes can be achieved upon this substrate. For example, this technique can be used for the study of shape and the arrangement of atomic steps modulated by the artificial strain field, though the experiments require a high temperature annealing such as 1230 °C [40].

The strain-distribution-controlled substrate is applied to Ge dot positioning. Fig. 6 shows an example of Ge island arrangement grown on Si(0 0 1). In this region, the oxide inclusions were buried using 1.5 μm width line patterns as the implantation

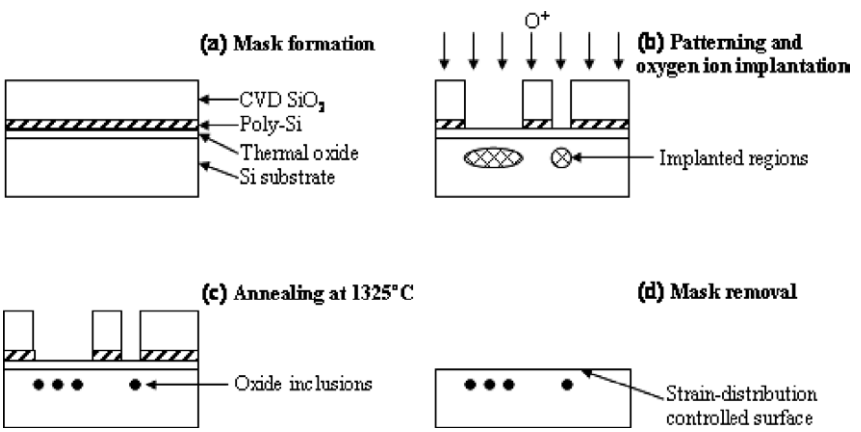

Fig. 5. Schematic illustration of the fabrication process of the strain-distribution-controlled substrates using spatially-selective oxygen ion implantation. (a) Multi-layered mask structure for the ion implantation. It consists of a thick CVD-grown SiO_2 layer for regulation of the ion implantation range, a polysilicon layer for etch-stop in the removal process of the CVD-SiO_2 layer, and a thin thermal SiO_2 layer for surface protection. (b) The CVD-SiO_2 mask patterned by optical lithography and oxygen ion implantion. (c) Annealing at high-temperatures, such as 1325 °C. (d) A strain-distribution-controlled surface after etching the whole mask layers.

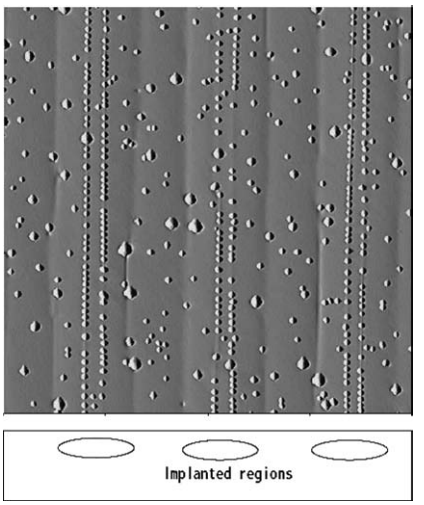

Fig. 6. AFM image ($8 \times 8\ \mu m^2$) of the surface after Ge island growth on a strain-distribution-controlled Si(1 0 0) surface. Ge islands were grown with a deposition coverage of 7.5 ML (6.3×10^{14} atoms/cm^2) at 550 °C using solid source molecular beam epitaxy. These islands (also called 'domes') are coherently strained on the surface.

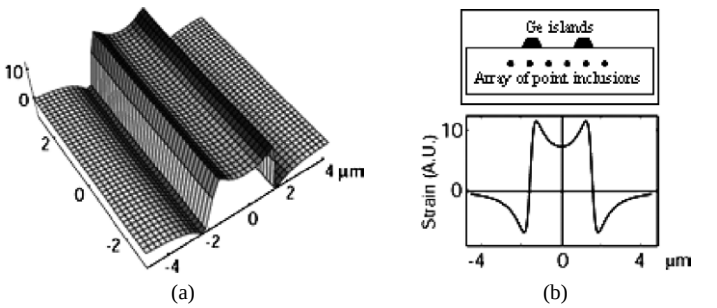

Fig. 7. Plot of the total strain function evaluated on the surface (a) and its cross section (b). The vertical scale is in a dimensionless unit CL^{-3}. In this calculation, we used an array of the point inclusions as shown in the inset of Fig. 7(b). The total strain function was defined as a sum of the individual strain functions corresponding to the single point inclusions. This model is justified by the small size of oxide inclusions that can be regarded as point stressors.

windows. This result demonstrates that artificial control of the strain field distribution is effective in forming a regular arrangement of coherently grown Ge quantum dots on Si(0 0 1).

The strain distribution was calculated from the trace of the two-dimensional strain-tensor evaluated in the surface plane that is expressed as [41]

$$\varepsilon(x, y) = \frac{C}{(x^2 + y^2 + L^2)^{3/2}} \left[\frac{3L^2}{(x^2 + y^2 + L^2)} - 1 \right], \tag{9}$$

where x and y are orthogonal distances in the surface plane from the place directly above a point inclusion at a depth L, and C is a constant related to elastic coefficients. Fig. 7 shows a 3D representation and a cross-section plot of the total strain function using Eq. (9) for the case of the linear array of point inclusions arranged in the implanted region as shown in the inset of Fig. 7(b). Note that two aligned lines of Ge dots are expected from the simulation result. The observation of mono-disperse Ge dots aligned in regular chains is probably due to diffusion and interaction effects along these lines. From micro-Raman spectroscopy measurements, we estimated that the maximum in-plane tensile strain is smaller than 0.01% [40,42]. This result suggests that strain effect to nanostructure self-assembly is remarkably large even if the strain is small.

The strain effect has a variety of aspects for self-assembled Ge nanostructures on Si surface other than the nucleation sites. A strain magnitude determines the size of Ge nanostructures and its symmetry influences the shape. Since the coherently grown Ge nanostructures induce in-plane strain on the substrate surface, interaction between the nanostructures are generated through the substrate strain. These aspects are well demonstrated in Ge nanowires on Si(113) surfaces [43].

3.3. Etching of buried dislocation networks

The use of buried dislocation networks to control the nucleation of nanostructures has been first demonstrated in metallic systems [44]. This approach needs a very fine-tuning of elastic fields and dislocation arrays. With standard lattice mismatch heteroepitaxy, networks may be very regular, but the dislocation spacing is directly related to the misfit of the layers [45]. The use of alloys to adjust the misfit to obtain a given spacing is difficult especially in semiconductors where the classical cross-hatched pattern is not enough regular [46].

It has been shown recently that specific molecular bonding of flat and clean Si surfaces may generate a buried array of dislocations with a controlled periodicity [47]. The principle of the process is shown in Fig. 8 and can be summarized as followed. After surface preparation and graduated scales patterning, a single silicon (001) wafer is cut into two 'twin' slices with an implantation process. These 'twin' surfaces are bonded again with a controlled relative in-plane rotation between them. A high-temperature annealing results in a self-organization of interfacial screw dislocations in a very regular square network [48,49]. These defects induce internal stresses in the bonded material, which propagate with an exponential decay

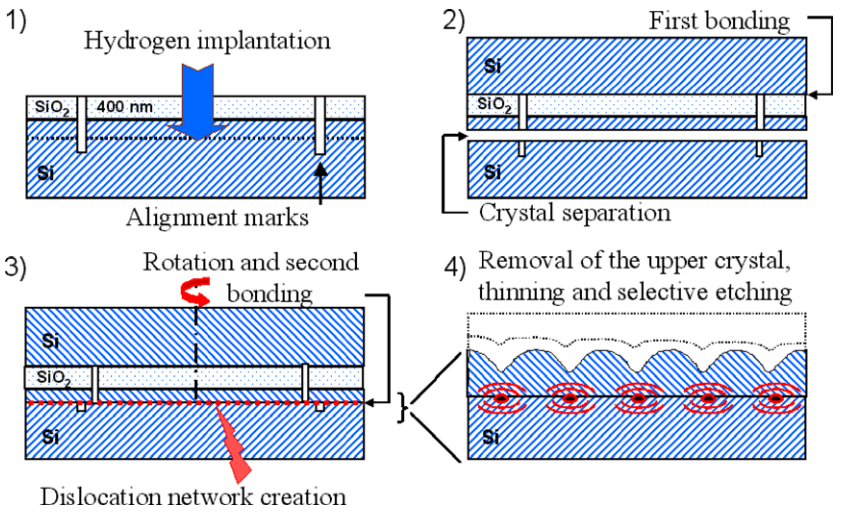

Fig. 8. Principle of the method used to obtain a twist-bonded sample with a controlled angle (a–c) and of the dislocation selective etching (d). Alignment marks are etched on the substrate that is implanted by hydrogen (a). A Si wafer is added (first bonding) to handle the sample during the separation process by annealing (b). The rotation is controlled with alignment marks under infrared light, and the second bonding is performed (c). This steps leads to the dislocation network formation. The wafer is thinned by conventional method then a strain-selective etching reveals the buried dislocation (d).

through the bonded layer up to the surface of the sample [50,51]. At the surface, the stress-maximum depends on the nature of the dislocation network (edge or screw components see [51]), and on the geometrical parameters such as the network periodicity Λ, the bonded layer thickness h, and the ratio h/Λ that defines the screening of the elastic fields. In the limit of small angles and for $a/2$ [1 1 0] Burgers vector (twist screw-dislocation), Λ is inversely proportional to the rotation angle ψ, which is controlled with an accuracy of 0.005° ($\Lambda \approx a/(\sqrt{2}\psi)$). It is thus possible to tune the periodicity of the dislocation network from a few nanometers up to micrometers. It is worth noting that low-angle bonding does not induce other defects at the interface, except some residual atomic steps. The direct Ge growth on smooth surface with buried screw-dislocation array has been attempted, but only a short-range order has been obtained. Etching has proven to be more selective to change first the surface morphology before the Ge growth. The upper silicon wafer and the oxide layer are then etched in a subsequent step [52,53] until the stress pattern is revealed at the surface (see Fig. 9). The etching solution consists of a strain-dependent mixture of oxidizing and complexing chemical reagents, typically a mixture of nitric, hydrofluoric and acetic acid, or a mixture of chromium oxide and hydrofluoric acid [53]. During the etching process, the local variations of the layer stress induce variations of the reaction rate, thus developing a final roughness correlated to the dislocation periodicity. The rate of the etching reaction is the product of a mobility term depending on the stress tensor by a non-linear kinetic term depending on the etching driving force. This driving force takes into account the free energy difference between solid and solvated silicon, the local elastic energy and an energy term related to the curvature of the surface [54] (see Section 2). Calculation of the local variations of the etching rate is difficult because the evolution of the surface morphology during etching induces modifications of the stress field. However, we have shown that this low reaction rate is sensitive to minor energy variations [53]. In the example shown in Fig. 9(a), the bonded layer thickness is decreased from an initial value of about 100 nm to less than 30 nm. The scanning tunneling microscopy (STM) image of a nano-patterned silicon surface consists of a square array of regularly spaced silicon nano-structures, with a lateral period of 25 nm consistent with the bonding angle of $\psi = 0.88°$, and an average height of about 5 nm. The periodicity of the initial buried dislocation network obtained before the thinning process is conserved as confirmed by grazing incidence X-ray diffraction. This surface preparation (nitric, hydrofluoric and acetic acid mixture) gives rounded and smooth bumps at the surface [53]. As shown in Fig. 9(b) for $\psi = 1°$, the use of different chemical etchings (chromium oxide and hydrofluoric acid mixture) [55] leads to narrower and less deep (1.5 nm) trenches and to a relatively large surface roughness at the top of the mesas (about 0.4 nm). According to the arguments developed in Section 2, the epitaxial growth on these two surfaces should not be similar. This behavior has been confirmed by the growth of 9 Å of germanium by molecular beam epitaxy at 490 °C (growth rate 0.7 Å/min) i.e. above the standard Stranski–Krastanov transition occurring at about 0.5–0.6 nm for the same temperature on a flat surface. For the rounded mesa, an original growth mode is observed with flat and rectangular germanium islands localized on top of the silicon bumps (see Fig. 9(c)). In contrast, the same deposition conditions on a flat substrate result in randomly distributed ‘hemispherical’ islands (16 nm in diameter). This original growth mode might be explained by the elastic relaxation of the germanium dots induced by the morphology of the silicon pattern. It has been confirmed recently by atomistic calculation

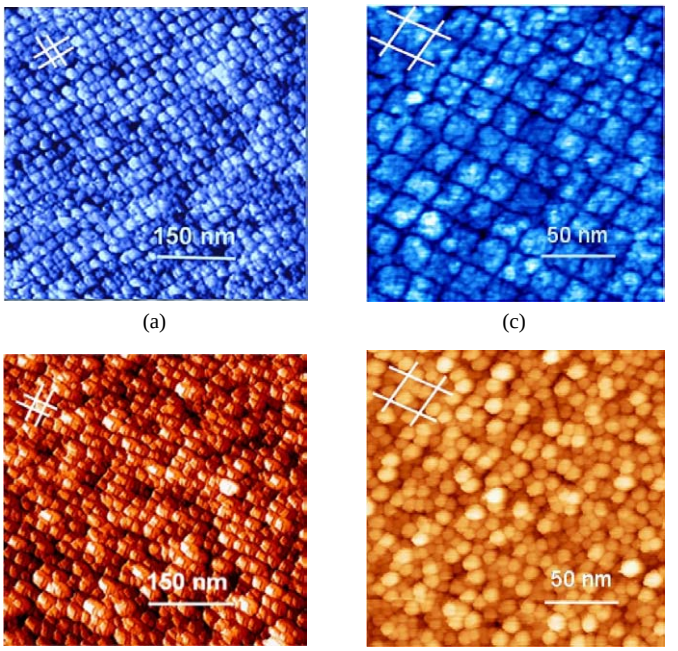

(a) (c)

(b) (d)

Fig. 9. STM images of the initial patterned Si-surface obtained by wafer bonding and strain selective etching (a, c), and of the deposition of 9 Å of Ge at 490 °C on these surfaces (b, d). For (a) (resp. (c)), the bonding angle is $\psi = 0.88°$ (resp. 1.005°), the nanostructures are 5 nm (1.5 nm) high and are separated by about 25 nm (22 nm). (a)-surface is etched with a mixture of nitric, hydrofluoric and acetic acid, and (c) with chromium oxide and hydrofluoric acid. Similar growth conditions give a single Ge dot per mesa in (b) and 4 to 5 dots per mesa in (d). Etched dislocation lines (drawn in white in the insets) are along the [1 1 0] and [1 −1 0] average directions of the bonded crystals.

that the standard 2D–3D transition of Ge quantum dots can be delayed or inhibited simply due to the elastic relaxation allowed by the edges of the mesas [56]. Rougher mesas shown in Fig. 9(b) give more nucleation sites that initiate the growth of 4 to 5 dots per mesa (see Fig. 9(d)) [57]. The dot coarsening occurs at the function of annealing temperature [55], and one dot per mesa is obtained for an annealing of about one hour at 725 °C. In this process, the depth of the trenches acts as a diffusion barrier to prevent large islands coalescence (the standard 'dome morphology' is not observed), and interdiffusion between the dots and the substrate plays probably a major role in the relaxation mechanism. The quantitative evaluation of the strain and composition in the dots can be performed by Anomalous Grazing Incidence X-Ray Diffraction (GIXRD) (see [58] and T. Metzger et al.'s article in this issue).

4. Conclusion

It has been shown that the interplay of *top-down* and *bottom-up* approaches that couple surface nanopatterning with self-organization opens new opportunities in future semiconductor technologies. In particular, the narrow size distribution can be induced by the regularity of the pattern, thus avoiding any statistical broadening in the measured properties. In the semiconductor surface nanostructuring presented in this paper, the effects of capillarity, growth rate anisotropy, entropy of mixing for alloys and strain relaxation directly determine the shape, density and location of deposited materials. Many other designs of specific surfaces not discussed in this paper (see for example the controlled step arrangements [59–61]) open new routes to nanostructure the surface for epitaxial growth. In this way, the morphology and surface stress engineering constitute a general approach to assembling nano-materials in well-defined networks, with the high density required by applications. This approach is of course not restricted to the deposition of semiconductor materials; it can also be used for organizing catalysts for nanotube or nanowire growths, magnetic materials for ultra-high density magnetic recording, as well as organic and non-organic molecules.

Acknowledgements

We thank our colleagues, current and former students, postdocs and visitors for their contributions. We greatly acknowledge Ing. P. Gentile, Dr. F. Leroy, Dr. F. Fournel for their contribution to Si surface nanostructuration at CEA; Dr F. Reinhardt for

MOCVD growth of QWR samples and Dr. A. Gustafsson for TEM images, Dr. Y. Homma (Tokyo University of Science), Dr. H. Omi, Dr. Kobayashi, Dr. Sumitomo (NTT Basic Research Laboratories), and Dr. D.J. Bottomley (Microsharp) for their collaboration at the Surface Science Research Group in NTT.

This work has been partly funded by the European Commission under the framework of the Network of Excellence 'SINANO' (Silicon-based Nanodevices, IST-506844).

References

[1] L. Jay Guo, New development of nanoimprint technology, J. Phys. D 37 (2004) R123.
[2] J.A. Meyer, I.D. Baikie, E. Kopatzki, R.J. Behm, Preferential island nucleation at the elbows of the Au(111) herringbone reconstruction through place exchange, Surf. Sci. 365 (1996) L647.
[3] P.M. Petroff, A.C. Gossard, W. Wiegmann, Structure of AlAs–GaAs interfaces grown on (100) vicinal surfaces by molecular beam epitaxy, Appl. Phys. Lett. 45 (1984) 620.
[4] S.Y. Shiryaev, F. Jensen, J.L. Hansen, J.W. Petersen, A.N. Larsen, Nanoscale structuring by misfit dislocations in $Si_{1-x}Ge_x$/Si epitaxial systems, Phys. Rev. Lett. 78 (1997) 503.
[5] J. Villain, A. Pimpinelli, Physique de la Croissance Cristalline, Collection Aléa-Saclay, ISBN 2-212-05800-4, Eyrolles, 1995.
[6] W.W. Mullins, Theory of thermal grooving, J. Appl. Phys. 28 (1957) 333.
[7] C. Herring, Diffusional viscosity of a polycrystalline solid, J. Appl. Phys. 21 (1950) 437.
[8] B. Yang, F. Liu, M.G. Lagally, Local strain-mediated chemical potential control of quantum dot self-organization in heteroepitaxy, Phys. Rev. Lett. 92 (2004) 025502.
[9] M. Borgstrom, V. Zela, W. Seifert, Quadruples of Ge dots grown on patterned Si surfaces, J. Cryst. Growth 259 (2003) 262.
[10] G. Jin, J.L. Liu, S.G. Thomas, Y.H. Luo, K.L. Wang, Controlled arrangement of self-organized Ge islands on patterned Si (0 0 1) substrates, Appl. Phys. Lett. 75 (1999) 2752.
[11] J.Y. Tsao, Material Fundamentals of Molecular Beam Epitaxy, Academic Press, Boston, 1993.
[12] H. Lee, J.A. Johnson, M.Y. He, J.S. Speck, P.M. Petroff, Strain-engineered self-assembled semiconductor quantum dot lattices, Appl. Phys. Lett. 78 (2001) 105.
[13] B.D. Gerardot, G. Subramanian, S. Minvielle, H. Lee, J.A. Johnson, W.V. Schoenfeld, D. Pine, J.S. Speck, P.M. Petroff, Self-assembling quantum dot lattices through nucleation site engineering, J. Cryst. Growth 236 (2002) 647.
[14] E. Kapon, D.M. Hwang, R. Bhat, Stimulated emission in semiconductor quantum wire heterostructures, Phys. Rev. Lett. 63 (1989) 430.
[15] G. Vermeire, I. Moerman, Z.Q. Yu, F. Vermaerke, P. Van Daele, P. Demeester, Atmospheric and low-pressure metalorganic vapor-phase epitaxial-growth of vertical quantum-wells and quantum-well wires on submicron gratings, J. Electron. Mater. 23 (1994) 121.
[16] A. Gustafsson, F. Reinhardt, G. Biasiol, E. Kapon, Low-pressure organometallic chemical vapour deposition of quantum wires on V-grooved substrates, Appl. Phys. Lett. 67 (1995) 3673.
[17] X.-L. Wang, M. Ogura, H. Matsuhata, Flow rate modulation epitaxy of AlGaAs/GaAs quantum wires on nonplanar substrate, Appl. Phys. Lett. 66 (1995) 1506.
[18] S. Koshiba, H. Noge, H. Akiyama, T. Inoshita, Y. Nakamura, A. Shimizu, Y. Nagamune, M. Tsuchiya, H. Kano, H. Sakaki, K. Wada, Formation of GaAs ridge quantum wire structures by molecular beam epitaxy on patterned substrates, Appl. Phys. Lett. 64 (1994) 363.
[19] A. Hartmann, L. Loubies, F. Reinhardt, E. Kapon, Self-limiting growth of quantum dot heterostructures on nonplanar {111}B substrates, Appl. Phys. Lett. 71 (1997) 1314.
[20] G. Biasiol, F. Reinhardt, A. Gustafsson, E. Martinet, E. Kapon, Structure and formation mechanisms of AlGaAs V-groove vertical quantum wells grown by low pressure organometallic chemical vapor deposition, Appl. Phys. Lett. 69 (1996) 2710.
[21] E. Martinet, A. Gustafsson, G. Biasiol, F. Reinhardt, E. Kapon, K. Leifer, Carrier quantum confinement in self-ordered AlGaAs V-groove quantum wells, Phys. Rev. B 56 (1997) 7096.
[22] G. Biasiol, E. Kapon, Mechanisms of self-ordering of quantum nanostructures grown on nonplanar surfaces, Phys. Rev. Lett. 81 (1998) 2962.
[23] G. Biasiol, A. Gustafsson, K. Leifer, E. Kapon, Mechanisms of self-ordering in nonplanar epitaxy of semiconductor nanostructures, Phys. Rev. B 65 (2002) 205306.
[24] C. Herring, in: W.E. Kingston (Ed.), The Physics of Powder Metallurgy, McGraw-Hill, New York, 1951, p. 143.
[25] M. Ozdemir, A. Zangwill, Theory of epitaxial growth onto nonplanar substrates, J. Vac. Sci. Technol. A 10 (1992) 684.
[26] G. Biasiol, K. Leifer, E. Kapon, Self-formation of semiconductor vertical quantum barriers by epitaxial growth on corrugated surfaces, Phys. Rev. B 61 (2000) 7223.
[27] M. Shinohara, M. Tanimoto, H. Yokoyama, N. Inoue, Wide terrace formation during metalorganic vapor phase epitaxy of GaAs, AlAs, and AlGaAs, Appl. Phys. Lett. 65 (1994) 1418.
[28] C.T. Black, K.W. Guarini, K.R. Milkove, S.M. Baker, T.P. Russel, M.T. Tuominen, Integration of self-assembled diblock copolymers for semiconductor capacitor fabrication, Appl. Phys. Lett. 79 (2001) 409.
[29] D.K. Yi, M.J. Kim, D.-Y. Kim, Surface relief grating induced colloidal crystal structures, Langmuir 18 (2002) 2019.
[30] S. Sun, C.B. Murray, D. Weller, L. Folks, A. Moser, Monodisperse FePt nanoparticles and ferromagnetic FePt nanocrystals superlattices, Science 287 (5460) (2000) 1989.
[31] P.A. Lewis, H. Ahmed, T. Sato, Silicon nanopillars formed with gold colloidal particle masking, J. Vac. Sci. Technol. B 16 (6) (1998) 2938.

[32] J.C. Hulteen, D.A. Treichel, M.T. Smith, M.L. Duval, T.R. Jensen, R.P.V. Duyne, Nanosphere lithography: size-tunable silver nanoparticle and surface cluster arrays, J. Phys. Chem. B 103 (1999) 3854.
[33] N. Li, M. Zinke-Allmang, Size-tunable Ge nano-particle arrays patterned on Si substrates with nanosphere lithography and thermal annealing, Jpn. J. Appl. Phys. Pt. 1 41 (7A) (2002) 4626.
[34] E.S. Györvary, A. O'Riordan, A.J. Quinn, G. Redmond, D. Pum, U.B. Sleytr, Biomimetic nanostructure fabrication: nonlithographic lateral patterning and self-assembly of functional bacterial S-layers at silicon supports, Nano Lett. 3 (2003) 315.
[35] U. Valbusa, C. Boragno, F. Buatier de Mongeot, Nanostructuring surfaces by ion sputtering, J. Phys.: Condens. Matter. 14 (2002) 8153.
[36] R. Gago, L. Vázquez, R. Cuerno, M. Varela, C. Ballesteros, J.M. Albella, Appl. Phys. Lett. 78 (2001) 3316.
[37] S. Facsko, T. Dekorsy, C. Koerdt, C. Trappe, H. Kurz, A. Vogt, H.L. Hartnagel, Formation of ordered nanoscale semiconductor dots by ion sputtering, Science 285 (1999) 1551.
[38] C. Teichert, M.G. Lagally, L.J. Peticolas, J.C. Bean, J. Tersoff, Stress-induced self-organization of nanoscale structures in SiGe/Si multilayer films, Phys. Rev. B 53 (1996) 16334.
[39] H. Omi, D.J. Bottomley, T. Ogino, Strain distribution control on the silicon wafer scale for advanced nanostructure fabrication, Appl. Phys. Lett. 80 (2002) 1073.
[40] H. Omi, D.J. Bottomley, Y. Homma, T. Ogino, S. Stoyanov, V. Tonchev, Shape of atomic steps on Si(111) under localized stress, Phys. Rev. B 66 (2002) 085303.
[41] J. Tersoff, C. Teichert, M.G. Lagally, Self-organization in growth of quantum dot superlattices, Phys. Rev. Lett. 76 (1996) 1675.
[42] H. Omi, D.J. Bottomley, Y. Homma, T. Ogino, Wafer-scale strain engineering on silicon for fabrication of ultimately controlled nanostructures, Phys. Rev. B 67 (2003) 115302.
[43] Z. Zhang, K. Sumitomo, H. Omi, T. Ogino, Influences of the Si(113) anisotropy on Ge nanowire formation and related island shape transition, Surf. Sci. 497 (2002) 93.
[44] H. Brune, M. Giovannini, K. Bromann, K. Kern, Self-organized growth of nanostructure arrays on strain-relief patterns, Nature 394 (1998) 451.
[45] G. Springholz, K. Wiesauer, Nanoscale dislocation patterning in PbTe/PbSe(001) lattice-mismatched heteroepitaxy, Phys. Rev. Lett. 88 (2002) 015507.
[46] E.A. Fitzgerald, M.T. Currie, S.B. Samavedam, T.A. Langdo, G. Taraschi, V. Yang, C.W. Leitz, M.T. Bulsara, Dislocations in relaxed SiGe/Si heterostructures, Phys. Status Solidi A 171 (1) (1999) 227.
[47] F. Fournel, H. Moriceau, B. Aspar, K. Rousseau, J. Eymery, J.-L. Rouviere, N. Magnea, Accurate control of the misorientation angles in direct wafer bonding, Appl. Phys. Lett. 80 (2002) 793.
[48] J. Eymery, F. Leroy, F. Fournel, GIXRD of nanoscale strain patterning in wafer bonding, Nucl. Instr. Meth. Phys. Res. B 200 (2003) 73.
[49] R. Bonnet, K. Rousseau, F. Fournel, Analyse du contraste d'un sous-joint de torsion (001) dans le silicium en MET à deux ondes, C. R. Physique 3 (2002) 657.
[50] A.E. Romanov, P.M. Petroff, J.S. Speck, Lateral ordering of quantum dots by periodic subsurface stressors, Appl. Phys. Lett. 74 (1999) 2280.
[51] A. Bourret, How to control the self-organization of nanoparticles by bonded thin layers, Surf. Sci. 432 (1999) 37.
[52] R.A. Wind, M.J. Murtagh, F. Mei, Y. Wang, M.A. Hines, S.L. Sass, Fabrication of nanoperiodic surface structures by controlled etching of dislocations in bicrystals, Appl. Phys. Lett. 78 (2001) 2205.
[53] F. Leroy, J. Eymery, P. Gentile, F. Fournel, Controlled surface nanopatterning with buried dislocation arrays, Surf. Sci. 545 (2003) 211.
[54] H.H. Yu, Z. Suo, Stress-dependent surface reactions and implications for a stress measurement technique, J. Appl. Phys. 87 (2000) 1211.
[55] P. Gentile, J. Eymery, F. Leroy, P. Perreau, J. Meziere, F. Fournel, Germanium growth on nanopatterned surface studied by STM, in: 14th International Conference on Crystal Growth, August 2004, J. Cryst. Growth, in press.
[56] C. Priester, On lateral organization of quantum dots on a prepatterned substrate, in: NATO ARW Proceedings, Kluwers Academic, June 2003.
[57] O.A. Louchev, Y. Sato, Influence of nanoscale substrate curvature on growth kinetics and morphology of surface nuclei, J. Appl. Phys. 84 (1998) 6673.
[58] J. Eymery, T. Schülli, P. Gentile, D. Buttard, F. Leroy, F. Fournel, Germanium quantum dot relaxation on nanopatterned Silicon surface, Appl. Phys. Lett., submitted for publication.
[59] T. Ogino, H. Hibino, Y. Homma, Step arrangement design and nanostructure self-organization on Si surfaces, Appl. Surf. Sci. 117/118 (1997) 642.
[60] T. Ogino, Self-organization of nanostructures on Si wafers using surface structure control, Surf. Sci. 386 (1997) 137.
[61] F. Lin, K. Sumitomo, Y. Homma, T. Ogino, STM observations of three-dimensional Ge islands on Si(111) surfaces with different step orientations and step-bunching conditions, Surf. Sci. 562 (2004) 15.